

Severe acute respiratory syndrome coronavirus papain-like protease: Structure of a viral deubiquitinating enzyme

Kiira Ratia*, Kumar Singh Saikatendu[†], Bernard D. Santarsiero*, Naina Barretto[‡], Susan C. Baker[‡], Raymond C. Stevens[§], and Andrew D. Mesecar*[¶]

*Center for Pharmaceutical Biotechnology and Department of Medicinal Chemistry and Pharmacognosy, University of Illinois, Chicago, IL 60607; Departments of [†]Cell Biology and [§]Molecular Biology, The Scripps Research Institute, La Jolla, CA 92037; and [‡]Department of Microbiology and Immunology, Loyola University Chicago Stritch School of Medicine, Maywood, IL 60153

Edited by Daniel E. Koshland, Jr., University of California, Berkeley, CA, and approved February 22, 2006 (received for review December 15, 2005)

Replication of severe acute respiratory syndrome (SARS) coronavirus (SARS-CoV) requires proteolytic processing of the replicase polyprotein by two viral cysteine proteases, a chymotrypsin-like protease (3CLpro) and a papain-like protease (PLpro). These proteases are important targets for development of antiviral drugs that would inhibit viral replication and reduce mortality associated with outbreaks of SARS-CoV. In this work, we describe the 1.85-Å crystal structure of the catalytic core of SARS-CoV PLpro and show that the overall architecture adopts a fold closely resembling that of known deubiquitinating enzymes. Key features, however, distinguish PLpro from characterized deubiquitinating enzymes, including an intact zinc-binding motif, an unobstructed catalytically competent active site, and the presence of an intriguing, ubiquitin-like N-terminal domain. To gain insight into the active-site recognition of the C-terminal tail of ubiquitin and the related LXGG motif, we propose a model of PLpro in complex with ubiquitin-aldehyde that reveals well defined sites within the catalytic cleft that help to account for strict substrate-recognition motifs.

membrane-associated protease | ubiquitin-like domain

In late 2002, severe acute respiratory syndrome (SARS) coronavirus (SARS-CoV) emerged as a dangerous pandemic agent that caused a highly contagious health threat with a mortality rate estimated at 10% (1–3). Although successful containment measures halted the spread of the virus, the possibility of future outbreaks of both SARS-CoV and related viruses warrants a continued search for new, effective antivirals. Replication of the SARS-CoV genome is mediated by nonstructural proteins (nsps 1–16) that assemble to generate the multifunctional, membrane-associated replicase complex. The nsps are encoded in two ORFs (ORF1a and ORF1b) encompassing >20 kb of the 5'-most region of the RNA genome. After infection, the SARS-CoV genomic RNA is released into the cytoplasm of the cell and translated into two long, overlapping polyproteins, pp1a and pp1ab (4) (Fig. 1). Processing of pp1a/1ab is carried out by two SARS-CoV proteases, the 3C-like protease (3CLpro) and the papain-like protease (PLpro) (5). Studies on structural and mechanistic aspects of 3CLpro have provided multiple avenues for high-throughput screening and structure-based design of antivirals targeted at the 3CLpro active site (6–9). On the other hand, the structure of the membrane-associated PLpro enzyme, from either SARS-CoV or any related coronavirus, has remained elusive. Unlike many coronaviruses that encode two PLpro paralogs (PLP1 or PLP2), SARS-CoV has a single copy of PLpro that cleaves pp1a at three sites at the N terminus (¹⁷⁷LNGG ↓ AVT₁₈₃, ⁸¹⁵LKGG ↓ API₈₂₁, and ²⁷³⁷LKGG ↓ KIV₂₇₄₃) to release nsp1, nsp2, and nsp3, respectively (5, 10) (Fig. 1).

PLpro resides within nsp3, which is a 213-kDa multidomain polypeptide that is membrane-associated (10). nsp3 also houses

a recently characterized phosphatase (11, 12), a transmembrane domain (10), a conserved acidic domain, and a Y domain of unknown function (Fig. 1). The transmembrane domains within nsp3, nsp4, and nsp6 are predicted to serve as the integral membrane scaffolding components that facilitate assembly of the double-membrane-associated replicase complex. Indeed, it has been demonstrated that coronavirus and arterivirus genome replication is largely confined to well defined, punctate areas along double-membrane vesicles originating from the endoplasmic reticulum (13–15). Recent studies indicate that assembly of the membrane-associated coronavirus replicase complex may involve subverting the process of autophagy to generate the double-membrane vesicles (16). Interestingly, we and others have shown that SARS-CoV PLpro is also a deubiquitinating enzyme (DUB) (17, 18). Thus, PLpro may have critical roles not only in proteolytic processing of the replicase complex but also in subverting cellular ubiquitination machinery to facilitate viral replication.

The amino acid sequence of the SARS-CoV PLpro domain of nsp3 bears all of the characteristic hallmarks of typical PLpros (clan CA), although there existed controversy concerning whether the enzyme exploited a Cys–His catalytic dyad (19) or a Cys–His–Asp catalytic triad (17). The most closely related cellular homologues in the PLpro clan include ubiquitin C-terminal hydrolase (UCH-L1), ubiquitin-specific protease 14 (USP14), and herpes-associated ubiquitin-specific protease (HAUSP, also known as USP 7) (20). Interestingly, the sequences at the three SARS-CoV replicase cleavage sites within pp1a that are recognized by PLpro bear strong resemblance to the C-terminal tail of ubiquitin (consensus sequence LXGG). Thus, it was hypothesized that SARS-CoV PLpro may have deubiquitinating activity (21). We and others purified the catalytic domain of PLpro and demonstrated that PLpro efficiently disassembles diubiquitin and branched polyubiquitin chains, cleaves ubiquitin-AMC substrates, and has de-ISGylating activity (17, 18). However, the role of these deubiquitinating and de-ISGylating activities in the virus replication cycle is currently unclear. A detailed understanding of the SARS-CoV PLpro domain is critical for the development of antiviral drugs and to

Conflict of interest statement: No conflicts declared.

This paper was submitted directly (Track II) to the PNAS office.

Abbreviations: SARS, severe acute respiratory syndrome; SARS-CoV, SARS coronavirus; PLpro, papain-like protease; nsp, nonstructural protein; Ubal, ubiquitin-aldehyde; Ubl, ubiquitin-like; PDB, Protein Data Bank; HAUSP, herpes-associated ubiquitin-specific protease; DUB, deubiquitinating enzyme.

Data deposition: The atomic coordinates and structure factors have been deposited in the Protein Data Bank, www.pdb.org (PDB ID code 2FE8).

[¶]To whom correspondence should be addressed at: Center for Pharmaceutical Biotechnology, University of Illinois, 900 South Ashland Avenue, M/C 870, Chicago, IL 60607. E-mail: mesecar@uic.edu.

© 2006 by The National Academy of Sciences of the USA

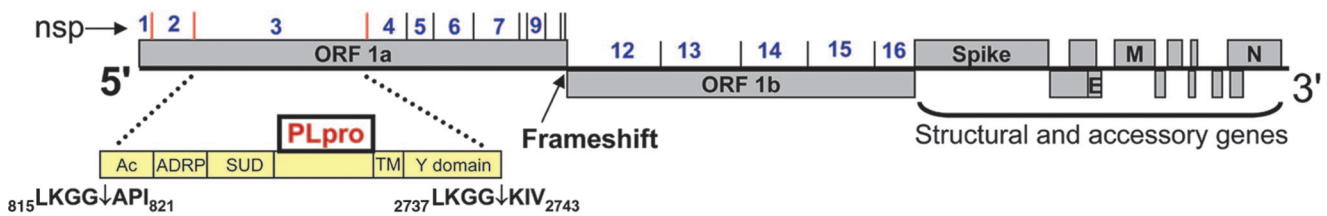


Fig. 1. Organization of the SARS-CoV genome. The location of the different nsps in ORF1a/1ab and the ORFs for structural and accessory proteins are marked. PLpro and 3CLpro cleavage sites are indicated by red and black vertical lines, respectively. (Inset) Arrangement of different functional subdomains of nsp3. The location of PLpro is highlighted in red. The N- and C-terminal cleavage sites that define the boundaries of nsp3 are indicated by ↓.

further our understanding of the role of this enzyme in the biogenesis of the coronavirus replicase complex.

Here we report the crystal structure of the SARS-CoV PLpro domain of nsp3 and describe important structural features including an intact catalytic triad, a zinc-binding domain, an N-terminal ubiquitin-like (Ubl) domain, and an overall resemblance to structures of known DUBs such as USP14 and HAUSP. To assess active-site recognition of the LXGG motif, we explore the interactions of a modeled ubiquitin moiety with key residues in the PLpro active site. To our knowledge, this structure is the first elucidated for a coronaviral PLpro and, in addition to lending structural support for proteolytic and DUB activities, offers a template for future drug-design efforts.

Results

Structure of SARS-CoV PLpro. The structure of the 35-kDa catalytic domain of PLpro (residues 1541–1855 of the SARS-CoV polyprotein) was determined to a resolution of 1.85 Å with a final R value of 20.1% ($R_{\text{free}} = 22.9\%$) (Table 1, which is published as supporting information on the PNAS web site). The PLpro monomer consists of four distinct domains, three of which form an extended right-hand architecture with distinct palm, thumb, and finger domains (Fig. 2A). The first 62 aa form an independent N-terminal domain, termed the Ubl domain, that is well separated from the other three domains and adopts a β -grasp fold similar to ubiquitin and Ubl domains of several proteins including ISG15, yeast yukD, elongin B, tubulin-binding cofactor

B, and modifier protein hub 1 (Fig. 2B). The thumb domain is formed by four prominent helices ($\alpha 4$ –7), and the palm is made up of a six-stranded β -sheet ($\beta 8$ –13) that slopes into the active site, which is housed in a solvent-exposed cleft between the thumb and palm domains (Fig. 2A). A four-stranded, twisted, anti-parallel β -sheet ($\beta 4$ –7) makes up the “fingers” domain. Two β -hairpins, at the fingertips region, contain four cysteine residues, which coordinate a zinc ion with tetrahedral geometry (Fig. 2A and C). The conformation of the cysteine side chains and the arrangement of the β -hairpins classify this zinc-binding site as a member of the circularly permuted, zinc-ribbon fold group (22). Biochemical evidence, computer modeling, and bioinformatics have predicted the presence of zinc-binding domains in coronavirus PLpros (19, 23), and we have demonstrated, through mutational analysis of the zinc-coordinating cysteines of SARS-CoV PLpro, that zinc-binding ability is essential for structural integrity and protease activity (17).

Comparison of the entire PLpro monomer with other structures in the Protein Data Bank (PDB) using the structure comparison service SSM (24) yielded several structural homologues from the cysteine protease superfamily. The most significant matches, based on the lowest rms deviation values, include the recently reported structure for USP14 (25), yeast Ubp6 (PDB ID code 1VJV), HAUSP (26), foot-and-mouth virus leader protease (27), and human Atg4B (28). The most striking similarities are with USP14 and HAUSP, both of which are cellular DUBs. Although sequence identities based on structure

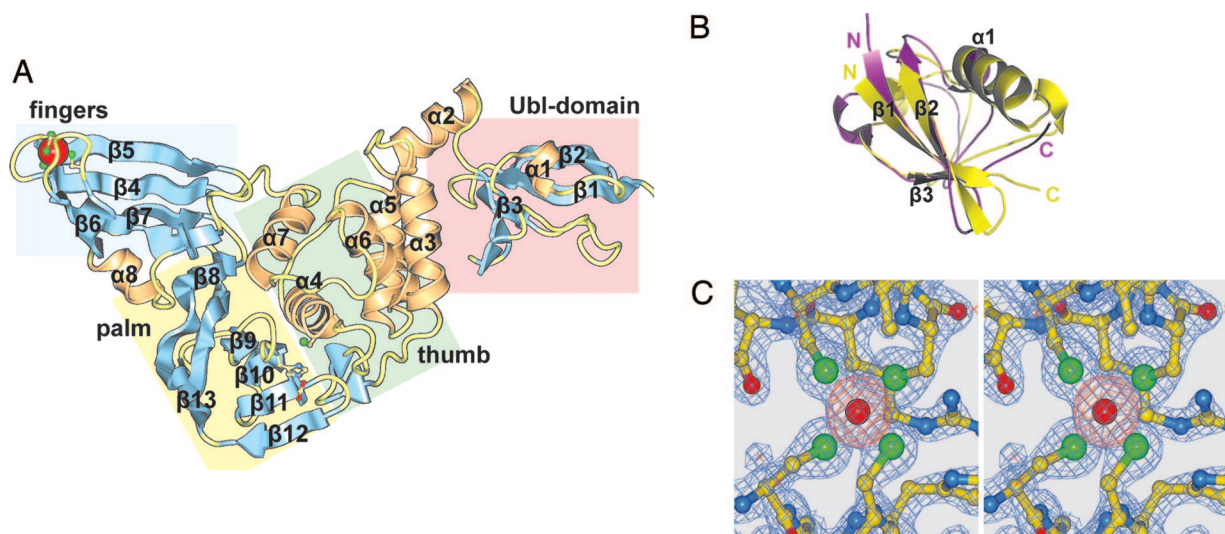


Fig. 2. Domain organization and structural motifs of SARS-CoV PLpro. (A) Locations of the Ubl (pink), thumb (green), palm (yellow), and fingers (pale blue) domains are indicated by colored boxes. α -Helices (orange) and β -sheets (blue) are numbered and depicted as ribbons. The zinc atom (red) is shown in space-fill representation, and zinc-coordinating cysteines and catalytic-triad residues are shown as ball-and-stick representations. (B) Structural superposition of residues 1–71 of ubiquitin (yellow) with residues 4–62 of the Ubl domain of SARS-CoV PLpro (violet). $\alpha 1$ and $\beta 1$ –3 of PLpro are labeled. The N and C termini of the aligned proteins are indicated. The rms deviation of 50 aligned residues is 2.12 Å at 16% sequence identity. (C) Stereoview of the electron density of the tetrahedrally coordinated zinc atom. A $2F_o - F_c$ map is contoured at 1.8σ (blue), and an $F_o - F_c$ omit map of the zinc atom is contoured at 8σ (red).

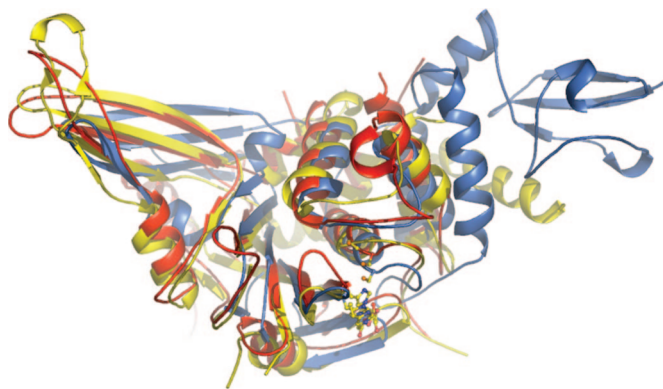


Fig. 3. Comparison of SARS-CoV PLpro with the cellular DUBs USP14 (PDB ID code 2AYN) and HAUSP (PDB ID code 1NB8). One hundred eighty-two residues of each protein, as chosen by the Web-based server SSM, were structurally aligned and superimposed. A ribbon diagram shows PLpro in blue, USP14 in red, and HAUSP in yellow. Catalytic triad residues are shown by ball-and-stick representations.

alignment of 182 residues of PLpro with USP14 and HAUSP are low (10% and 11%, respectively), the topologies of the structural superpositions are remarkably similar, with corresponding rms deviations of alignment of 2.7 Å and 3.2 Å (Fig. 3).

Active-Site Conformation and Access. The active site of PLpro consists of a catalytic triad of cysteine, histidine, and aspartic acid residues, consistent with catalytic triads found in many PLpros (29) (Fig. 4A). The catalytic cysteine (C112) is located at the base of $\alpha 4$ of the thumb domain and is located 3.7 Å from the triad histidine (H273), which is situated at the base of the palm domain (Figs. 2 and 4A). Despite initial proposals that coronavirus PLpros function with only a Cys–His dyad (19), our structure clearly identifies an aligned, functional triad, as was recently proposed and demonstrated from modeling (21) and mutagenesis (17) studies. In the structure of PLpro, the aspartic acid residue (D287) is situated in a classic triad formation, within hydrogen-bonding distance (2.7 Å) of H273. The catalytic triad aligns well with that of other PLpros, including USP14 (25), but not with that of HAUSP, whose active site requires substrate

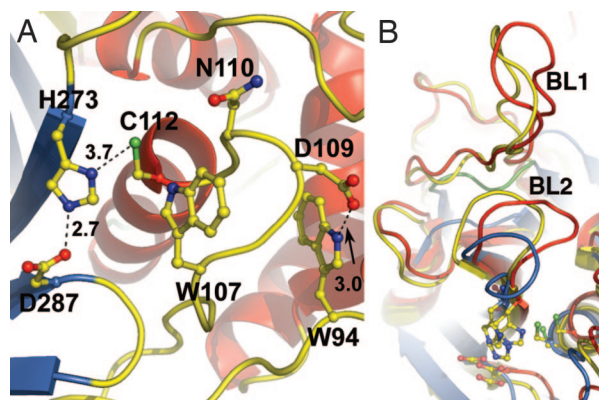


Fig. 4. The SARS-CoV PLpro and USP14 active sites. (A) SARS-CoV PLpro catalytic triad residues, C112, H273, and D287, and other important active-site residues. Distances between residues are indicated in angstroms. The hydrogen bond between D109 and W97 is indicated by an arrow. (B) Comparison of USP14 and SARS-CoV PLpro BL1 and BL2 loop regions. Corresponding regions of unbound USP14 (red), Ubal-complexed USP14 (yellow), and PLpro (blue) are shown superimposed. The BL1 and BL2 loop regions are indicated. The BL1 loop region of PLpro is colored in green. The catalytic triad residues are shown by a ball-and-stick representation.

binding for the catalytic cysteine to align into an active conformation as part of a possible regulatory mechanism (26).

An important feature of serine and cysteine protease active sites is the presence of an oxyanion hole to stabilize negative charge formation during peptide hydrolysis. The general mechanism of peptide cleavage involves the formation of two negatively charged tetrahedral intermediates. The amino groups of asparagine and glutamine side-chain residues in several PLpros are known to provide the stabilization forces required of oxyanion holes (29). Analysis of the SARS-CoV PLpro structure reveals that the oxyanion hole contains a tryptophan residue (W107) in the corresponding position (Fig. 4A), as suggested by a recent modeling study (21). Because it is likely that the indole-ring nitrogen of W107 can act as a hydrogen-bond donor to the developing negative charge on the tetrahedral intermediate, we mutated this residue to an alanine, tested enzymatic activity in trans-cleavage assays, and found the mutant to be completely inactive (Fig. 7, which is published as supporting information on the PNAS web site). In addition to W107, an asparagine residue, N110, which is highly conserved among coronavirus PLP2s, is situated above the catalytic cysteine and may also contribute to oxyanion hole stabilization.

Mutagenesis studies indicate that access to the PLpro active site is limited to substrates with diglycine residues in the P2 and P1 sites (17). Several important structural features dictate access to the narrow active site, including a series of loops surrounding the area. One such loop is situated at the mouth of the active site and is comprised of residues 103–110. W107, which we propose acts to stabilize the oxyanion hole, protrudes from this loop into the active site (Fig. 4A). An important hydrogen-bond interaction between the side chains of D109 on the loop and W94 behind the loop appears to prevent collapse of the loop into the active site. A PLpro W94A mutant is inactive in trans-cleavage assays (Fig. 7), indicating that the hydrogen bond contributed by W94 to D109 is most likely essential for maintaining an accessible active site.

Hu *et al.* (25) described two “blocking loops,” designated BL1 and BL2, that are important structural features of USP14. BL1 and BL2 block access to the active site and palm regions when USP14 is in an unbound state. However, upon formation of the ubiquitin–aldehyde (Ubal) complex the loops are displaced and move away from the active site. These loops are hypothesized to serve a regulatory role in modulating the deubiquitinating activity of USP14 (25). HAUSP contains similar loop regions, but its BL1 loop is largely disordered, and its BL2 loop is in an open state when HAUSP is uncomplexed (26). When compared with both the uncomplexed and ubiquitin aldehyde-bound structures of USP14, it is strikingly evident that, although PLpro possesses a similar BL2 loop, it completely lacks the much larger BL1 loop (Fig. 4B). In contrast to an extended, 22-aa loop between β -strands as observed within USP14, the corresponding region in PLpro is a short, 6-aa-long bend in strand $\beta 8$ that turns behind the palm as opposed to protruding into the ubiquitin-binding region. The BL2 loop of PLpro (residues 267–272) is similar in length to the BL2 loops of both HAUSP and USP14, all of which contain two glycines on either stem (G267 and G272). These glycines are 2 of 11 residues conserved among PLpro, USP14, and HAUSP and may be important for imparting flexibility to the loop region. Comparison of the BL2 loop of PLpro with that of USP14 in bound and unbound conformations reveals that the PLpro BL2 loop more closely resembles that of the USP14–ubiquitin complex, indicating that the BL2 loop of PLpro is likely in an open state (Fig. 4B).

Interactions of PLpro with Ubiquitin. It was recently demonstrated that the PLpro catalytic domain of nsp3 has deubiquitinating activity *in vitro* (17, 18). To gain insight into the interactions of the PLpro active site with ubiquitin, we used both the HAUSP

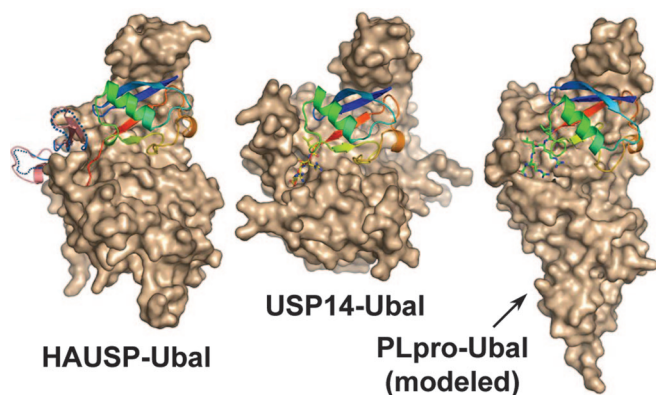


Fig. 5. Comparison of the ubiquitin-binding surfaces of HAUSP, USP14, and PLpro based on modeling studies. For modeling ubiquitin into the SARS-CoV PLpro active site, the structures of the Ubal-bound forms of HAUSP (1nbf) and USP14 (2ayo) were superimposed onto the PLpro structure and analyzed. Contacts at the C-terminal tail of ubiquitin and two interacting surfaces of the PLpro palm domain were manually edited and minimized by using CNS. The ubiquitin molecule is shown as a ribbon diagram.

(26) and USP14 (25) structures complexed with Ubal to model the ubiquitin molecule into the corresponding binding site of PLpro (Fig. 5). Because there are no loops occluding the active site in the apo form of PLpro, the C-terminal tail extension of ubiquitin is easily accommodated in the active site. Although slightly shorter than that of HAUSP or USP14, the fingers region of PLpro appears to be large enough to cradle the body of ubiquitin without significant structural clashes (Fig. 5).

Based on the consensus sequence of the three PLpro cleavage sites in the SARS polyprotein and biochemical studies addressing substrate preference, it has been demonstrated that an LXGG motif at the P4–P1 positions of the substrate is essential for recognition and cleavage (17, 30). There appear to be no preferences for the P' positions or for residues N-terminal to P4. It is not surprising then that PLpro is able to cleave after the four C-terminal residues of ubiquitin, LRGG. A positively charged arginine at the P3 position of the ubiquitin substrate correlates well with positively charged lysines at two of three P3 positions in PLpro polyprotein substrates.

The docking studies of Ubal into the PLpro active site reveal that two tyrosine residues (Y113 and Y274) are partially responsible for the strict requirement for glycines at the P1 and P2 positions of PLpro substrates (Fig. 6A). Both tyrosines are conserved in HAUSP and USP14. Coronavirus PLP2-like en-

zymes with substrate specificities requiring a glycine at P1 and either a glycine or alanine at P2 also contain a tyrosine at a position analogous to Y274 and a bulky aromatic group at a position corresponding to Y113 (23, 31, 32). It is also important to note that aromatic residues neighboring the catalytic cysteine are very common in PLpros because they can serve to enhance the nucleophilicity of the cysteine residue (33). Residues N110 and L163 also appear to contribute to P1 specificity by hovering above the active site in a position that could sterically block residues larger than a glycine (Fig. 6).

Stabilization of the P3 backbone is contributed by an additional tyrosine, Y265, which corresponds to histidines in both USP14 and HAUSP. This residue sits below the P3 subsite and may stabilize the backbone of the substrate in the active site by hydrogen bonding with the P3 carbonyl, as well as direct the bulky P3 side chain out of the cleft (Fig. 6A). An alanine mutation at this position in SARS-CoV PLpro (Y265A) results in an inactive enzyme (17). Because of spatial requirements, the P5 arginine is also oriented upward and appears to be stabilized in part by a negative patch on the thumb domain created by two residues, E168 and D165, which are conserved in USP14 and HAUSP (Fig. 6A and B). E168 is in position to form a salt bridge with the P5 arginine side chain, whereas D165 hydrogen bonds to the P4 backbone amide as in HAUSP and USP14 (Fig. 6A).

The requirement for a leucine residue at the P4 position of PLpro substrates can be explained by the presence of a small hydrophobic crevice created by the side chains of P249, T302, and Y265 that lie underneath the bound substrate (Fig. 6A). We have shown through mutagenesis and trans-cleavage assays that substitution of leucine for an alanine residue at the P4 position is not well tolerated (17). Leucine may be serving as a hydrophobic anchor that helps to align the substrate into an orientation that is favorable for catalysis. It has been shown that even slight alterations, e.g., 1 Å, in active-site geometries can have profound effects on catalytic rates (34). Thus, an alanine residue at the P4 position may be unable to properly align the substrate for cleavage.

Many of the interactions that can potentially stabilize Ubal in the catalytic cleft of PLpro stem from hydrogen bonds to the backbone atoms of Ubal. In our model, at least six such hydrogen bonds are observed between the main-chain atoms of P1 to P4 of Ubal and the backbone and side chain atoms of PLpro active-site residues (Fig. 6A). The same interactions are also seen in the active sites of USP14 (25) and HAUSP (26). Additional stabilization of Ubal by PLpro is provided by the oxyanion hole. The positioning of the thiohemiacetal hydroxyl of the reacted Ubal, which would mimic an oxyanion intermediate, is found

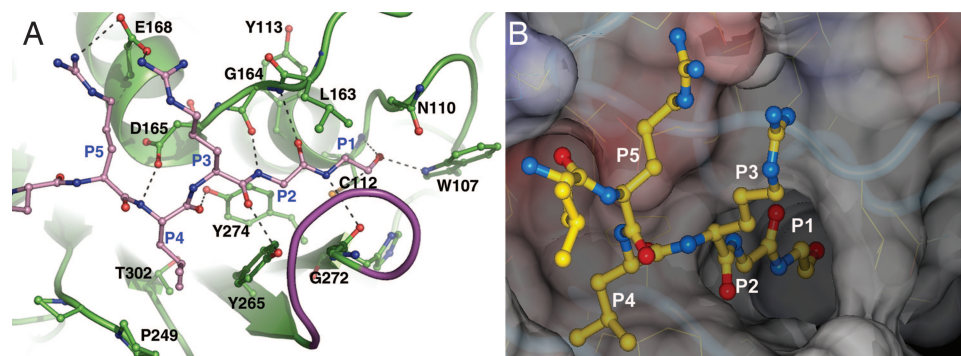


Fig. 6. Hypothetical model of the interaction of ubiquitin with the PLpro active site based on the structures of HAUSP and USP14 complexed with Ubal. (A) Modeled interactions between the C-terminal tail of Ubal (pink backbone) and the PLpro (green backbone). PLpro residues are labeled in black, and the ubiquitin side chains are labeled P1–P5 in blue. Proposed hydrogen bonds are indicated by dashed lines. The BL2 loop is shown in magenta. (B) A surface representation of the PLpro active-site tunnel is shown complexed with modeled Ubal. The Ubal is shown by a ball-and-stick representation. The P1–P5 positions of Ubal are labeled.

within hydrogen-bonding distance of the proposed oxyanion hole residue W107 and the backbone amide nitrogen of C112.

Discussion

The x-ray structure of SARS-CoV PLpro now provides a clearer picture of the structural basis for the proteolytic processing at the LXGG consensus cleavage site (Fig. 1) and helps to explain its mechanism of deubiquitination in molecular detail. Lindner *et al.* (18) showed that SARS-CoV PLpro, in addition to its proteolytic and deubiquitinating functions, is also capable of effectively de-ISGylating protein conjugates by recognizing and cleaving the C-terminal sequence -LRLRGG of ISG15. Induction of ISG15 and its subsequent conjugation to proteins confer protection to cells during infection by viruses (35, 36). As a potential protective measure, a number of viruses are known to interfere with ISG15 or ubiquitin-conjugation pathways. For example, the NS1B protein of influenza B virus prevents ISGylation of proteins by binding to ISG15 (37). Like SARS-CoV PLpro, a number of viral proteases have also been shown to deconjugate Ubl modifiers, including proteases from herpes simplex virus 1 and homologues (38, 39), African swine fever virus (40), and adenovirus (41). By analogy, these parallel studies strongly suggest the possibility that SARS-CoV uses similar mechanisms of protection against ubiquitination or ISGylation.

One of the most surprising observations that stems from the x-ray structure of PLpro is that the N-terminal domain of SARS-CoV PLpro adopts a structural fold similar to both ubiquitin and ISG15, which classifies it as a Ubl domain (Fig. 2B). Interestingly, this domain is also present in a number of cellular DUBs, including full-length USP14 and Ubp6, the yeast homologue of USP14 (42). Although the significance of this domain is not well established, it has been demonstrated that the presence of the Ubl domain in USP14 and Ubp6 serves a regulatory function by mediating interactions between these DUBs and specific components of the proteasome (25, 43). Comparisons of DUB activities between wild-type and mutant Ubp6 lacking the Ubl domain reveal that these associations are responsible for a 300-fold increase in catalytic rate and serve to activate the enzyme (43).

We measured the rate of deubiquitinating activity of SARS-CoV PLpro *in vitro* (17) and found that it has significantly higher activity than both HAUSP (26) and USP14 (44). SARS-CoV PLpro has a catalytic efficiency, k_{cat}/K_m , of $75,000 \text{ M}^{-1}\text{s}^{-1}$ compared with a value of $2,200 \text{ M}^{-1}\text{s}^{-1}$ for HAUSP. USP14 has a k_{cat}/K_m value of $107 \text{ M}^{-1}\text{s}^{-1}$ (44) but is substantially activated through association with the proteasome (45).

Because PLpro is localized to the membrane-bound replicase complex (10), it is unclear whether only viral or possibly cellular proteins are potential substrates for PLpro DUB activity. The crystal structure reveals that the active site is both unobstructed and in a catalytically competent configuration when compared with USP14 and HAUSP, indicating that activation may not be a requirement for efficient, PLpro DUB activity. It is intriguing to consider that the Ubl-like domain of PLpro may instead act as a sort of “decoy” or “lure” to detract cellular ubiquitinating enzymes from other viral proteins, or it may mediate protein-protein interactions between the replicase components. Although the structures of the catalytic cores of USP14 (25) and Ubp6 (PDB ID code 1VJV) have been determined, to our knowledge this study provides the first structure of an intact Ubl domain connected to the signature three-domain, thumb-palm-fingers architecture of DUBs. The x-ray structure of SARS-CoV PLpro engenders several new avenues for further studies aimed at addressing the multiple functions of this provocative enzyme.

Conclusion

The x-ray structure of SARS-CoV PLpro provides important structural and mechanistic insights into the family of coronavirus

PLpros. Future studies of SARS-CoV PLpro will be aimed at elucidating the potential dual role of this enzyme in proteolytic processing of the replicase polyprotein and deubiquitinating activity of viral and cellular proteins during viral replication. This structure also expands the available arsenal of structural templates of different SARS proteins that can be targeted for inhibition by therapeutic compounds and thus disrupt the replication of SARS-CoV.

Materials and Methods

Crystallization. Untagged, native SARS-CoV PLpro (polyprotein residues 1541–1855) was expressed and purified as previously described (17). Crystallization was performed at 25°C by using the hanging-drop vapor-diffusion technique. A series of crystallization grids were prepared by mixing ≈ 2.5 –10 mg/ml PLpro in 20 mM Tris, pH 7.5/10 mM DTT, with equal volumes of reservoir solution containing 100 mM sodium citrate (pH 5.2–5.6) and 1.2–1.5 M ammonium sulfate. The majority of crystals were typically macroscopically twinned. Single, larger crystals suitable for data collection were eventually obtained and were soaked in a cryosolution consisting of reservoir solution and 20% glycerol. Crystals were flash-frozen in liquid nitrogen and then transferred into a dry nitrogen stream at 100 K for x-ray data collection. Isomorphous replacement derivatives were prepared by soaking crystals directly in the cryosolution supplemented with 20 mM $\text{K}_2\text{Pt}(\text{CN})_4 \cdot \text{XH}_2\text{O}$ or 50 mM KBr.

X-Ray Data Collection, Processing, and Structure Determination. The native, Pt, and Br x-ray data sets were collected at Southeast Regional Collaborative Access Team 22-ID and 22-BM beamlines and National Institutes of General Medical Sciences General Medicine/Collaborative Access 23-ID beamline at the Advanced Photon Source, Argonne National Laboratory. Native and Pt data sets were collected at $\lambda = 1.000 \text{ \AA}$, and the Br data set was collected at $\lambda = 0.921 \text{ \AA}$. Data were processed and scaled by using the HKL2000 program suite (46). Crystals belonged to the space group C2, with three monomers in the asymmetric unit. The Matthews coefficient, V_M , was calculated as 3.0, corresponding to 58% solvent content. All data sets were found to be isomorphous. Phases were determined by isomorphous replacement of the native data with the Pt derivative data to 2.0 Å by using SOLVE (47), which located six Pt atoms in the asymmetric unit, with partial occupancy of 0.14–0.42 and an overall mean figure of merit of 0.29 and a Z score of 58.55. Phases were subsequently improved by using RESOLVE (48) to a mean overall figure of merit of 0.64. Initial density maps were traceable by ARP/WARP (49), which built three partial fragments in the asymmetric unit. Manual rebuilding in O (50) and initial refinement with CNS (51) generated a starting model for further refinement by using the Br data set, which provided the most complete data to 1.85 Å. The Br data were used only for model refinement and not for phasing purposes. The three monomers in the asymmetric unit superimpose with an rms deviation of 1.2–1.6 Å for all $\text{C}\alpha$ atoms. The greatest deviations stem from an overall flexibility of the fingers domain, particularly the zinc-binding region. Distances and interactions discussed in the text are consistent in all three monomers. For simplicity, all figures were generated from chain A, with the exception of Fig. 2C, which was generated from chain B because of the quality of the electron density in the region depicted. Figures were created by using NOC (<http://noc.ibp.ac.cn>) and PYMOL (<http://pymol.sourceforge.net>).

Site-Directed Mutagenesis and SARS-CoV Trans-Cleavage Assays. Site-directed mutagenesis and trans-cleavage assays were performed as described previously (10).

We acknowledge Dalia Jukneliene for excellent technical assistance; Vanitha Subramanian for help with crystallization and imaging; and Peter Kuhn, Michael Buchmeier, and Ben Neuman for scientific discussions and support. We gratefully acknowledge the synchrotron beamline personnel at Advanced Photon Source (Southeast Regional Collaborative Access Team) 22-ID and 22-BM beamlines. Portions of this research were carried out at the General Medicine and Cancer Institutes Collaborative Access Team (GM/CA-CAT) beamlines of the Advanced Photon Source. GM/CA-CAT has been funded in whole or in part with funds from the National Cancer Institute (Y1-CO-1020)

1. Rota, P. A., Oberste, M. S., Monroe, S. S., Nix, W. A., Campagnoli, R., Icenogle, J. P., Penaranda, S., Bankamp, B., Maher, K., Chen, M. H., et al. (2003) *Science* **300**, 1394–1399.
2. Ksiazek, T. G., Erdman, D., Goldsmith, C. S., Zaki, S. R., Peret, T., Emery, S., Tong, S., Urbani, C., Comer, J. A., Lim, W., et al. (2003) *N. Engl. J. Med.* **348**, 1953–1966.
3. Kuiken, T., Fouchier, R. A., Schutten, M., Rimmelzwaan, G. F., van Amerongen, G., van Riel, D., Laman, J. D., de Jong, T., van Doornum, G., Lim, W., et al. (2003) *Lancet* **362**, 263–270.
4. Ziebuhr, J. (2004) *Curr. Opin. Microbiol.* **7**, 412–419.
5. Thiel, V., Ivanov, K. A., Putics, A., Hertzog, T., Schelle, B., Bayer, S., Weissbrich, B., Snijder, E. J., Rabenau, H., Doerr, H. W., et al. (2003) *J. Gen. Virol.* **84**, 2305–2315.
6. Blanchard, J. E., Elowe, N. H., Huitema, C., Fortin, P. D., Cechetto, J. D., Eltis, L. D. & Brown, E. D. (2004) *Chem. Biol.* **11**, 1445–1453.
7. Anand, K., Ziebuhr, J., Wadhvani, P., Mesters, J. R. & Hilgenfeld, R. (2003) *Science* **300**, 1763–1767.
8. Yang, H., Yang, M., Ding, Y., Liu, Y., Lou, Z., Zhou, Z., Sun, L., Mo, L., Ye, S., Pang, H., et al. (2003) *Proc. Natl. Acad. Sci. USA* **100**, 13190–13195.
9. Ghosh, A. K., Xi, K., Ratia, K., Santarsiero, B. D., Fu, W., Harcourt, B. H., Rota, P. A., Baker, S. C., Johnson, M. E. & Mesecar, A. D. (2005) *J. Med. Chem.* **48**, 6767–6771.
10. Harcourt, B. H., Jukneliene, D., Kanjanahaluethai, A., Bechill, J., Severson, K. M., Smith, C. M., Rota, P. A. & Baker, S. C. (2004) *J. Virol.* **78**, 13600–13612.
11. Saikatendu, K. S., Joseph, J. S., Subramanian, V., Clayton, T., Griffith, M., Moy, K., Velasquez, J., Neuman, B. W., Buchmeier, M. J., Stevens, R. C. & Kuhn, P. (2005) *Structure (Cambridge)* **13**, 1665–1675.
12. Snijder, E. J., Bredenbeek, P. J., Dobbe, J. C., Thiel, V., Ziebuhr, J., Poon, L. L., Guan, Y., Rozanov, M., Spaan, W. J. & Gorbalenya, A. E. (2003) *J. Mol. Biol.* **331**, 991–1004.
13. Gosert, R., Kanjanahaluethai, A., Egger, D., Bienz, K. & Baker, S. C. (2002) *J. Virol.* **76**, 3697–3708.
14. Pedersen, K. W., van der Meer, Y., Roos, N. & Snijder, E. J. (1999) *J. Virol.* **73**, 2016–2026.
15. Shi, S. T., Schiller, J. J., Kanjanahaluethai, A., Baker, S. C., Oh, J. W. & Lai, M. M. (1999) *J. Virol.* **73**, 5957–5969.
16. Prentice, E., Jerome, W. G., Yoshimori, T., Mizushima, N. & Denison, M. R. (2004) *J. Biol. Chem.* **279**, 10136–10141.
17. Barretto, N., Jukneliene, D., Ratia, K., Chen, Z., Mesecar, A. D. & Baker, S. C. (2005) *J. Virol.* **79**, 15189–15198.
18. Lindner, H. A., Fotouhi-Ardakani, N., Lytvyn, V., Lachance, P., Sulea, T. & Menard, R. (2005) *J. Virol.* **79**, 15199–15208.
19. Herold, J., Siddell, S. G. & Gorbalenya, A. E. (1999) *J. Biol. Chem.* **274**, 14918–14925.
20. Barrett, A. J. & Rawlings, N. D. (2001) *Biol. Chem.* **382**, 727–733.
21. Sulea, T., Lindner, H. A., Purisima, E. O. & Menard, R. (2005) *J. Virol.* **79**, 4550–4551.
22. Krishna, S. S., Majumdar, I. & Grishin, N. V. (2003) *Nucleic Acids Res.* **31**, 532–550.
23. Ziebuhr, J., Thiel, V. & Gorbalenya, A. E. (2001) *J. Biol. Chem.* **276**, 33220–33232.
24. Krissinel, E. & Henrick, K. (2004) *Acta Crystallogr. D* **60**, 2256–2268.
25. Hu, M., Li, P., Song, L., Jeffrey, P. D., Chenova, T. A., Wilkinson, K. D., Cohen, R. E. & Shi, Y. (2005) *EMBO J.* **24**, 3747–3756.
26. Hu, M., Li, P., Li, M., Li, W., Yao, T., Wu, J. W., Gu, W., Cohen, R. E. & Shi, Y. (2002) *Cell* **111**, 1041–1054.
27. Guarne, A., Hampoelz, B., Glaser, W., Carpena, X., Tormo, J., Fita, I. & Skern, T. (2000) *J. Mol. Biol.* **302**, 1227–1240.
28. Sugawara, K., Suzuki, N. N., Fujioka, Y., Mizushima, N., Ohsumi, Y. & Inagaki, F. (2005) *J. Biol. Chem.* **280**, 40058–40065.
29. Johnston, S. C., Larsen, C. N., Cook, W. J., Wilkinson, K. D. & Hill, C. P. (1997) *EMBO J.* **16**, 3787–3796.
30. Han, Y. S., Chang, G. G., Juo, C. G., Lee, H. J., Yeh, S. H., Hsu, J. T. & Chen, X. (2005) *Biochemistry* **44**, 10349–10359.
31. Kanjanahaluethai, A., Jukneliene, D. & Baker, S. C. (2003) *J. Virol.* **77**, 7376–7382.
32. Lim, K. P., Ng, L. F. & Liu, D. X. (2000) *J. Virol.* **74**, 1674–1685.
33. Berti, P. J. & Storer, A. C. (1995) *J. Mol. Biol.* **246**, 273–283.
34. Mesecar, A. D., Stoddard, B. L. & Koshland, D. E., Jr. (1997) *Science* **277**, 202–206.
35. Kim, K. I. & Zhang, D. E. (2003) *Biochem. Biophys. Res. Commun.* **307**, 431–434.
36. Ritchie, K. J., Hahn, C. S., Kim, K. I., Yan, M., Rosario, D., Li, L., de la Torre, J. C. & Zhang, D. E. (2004) *Nat. Med.* **10**, 1374–1378.
37. Yuan, W. & Krug, R. M. (2001) *EMBO J.* **20**, 362–371.
38. Schlieker, C., Korb, G. A., Kattenhorn, L. M. & Ploegh, H. L. (2005) *J. Virol.* **79**, 15582–15585.
39. Kattenhorn, L. M., Korb, G. A., Kessler, B. M., Spooner, E. & Ploegh, H. L. (2005) *Mol. Cell* **19**, 547–557.
40. Andres, G., Alejo, A., Simon-Mateo, C. & Salas, M. L. (2001) *J. Biol. Chem.* **276**, 780–787.
41. Balakirev, M. Y., Jaquinod, M., Haas, A. L. & Chroboczek, J. (2002) *J. Virol.* **76**, 6323–6331.
42. Wyndham, A. M., Baker, R. T. & Chelvanayagam, G. (1999) *Protein Sci.* **8**, 1268–1275.
43. Leggett, D. S., Hanna, J., Borodovsky, A., Crosas, B., Schmidt, M., Baker, R. T., Walz, T., Ploegh, H. & Finley, D. (2002) *Mol. Cell* **10**, 495–507.
44. Chernova, T. A., Allen, K. D., Wesoloski, L. M., Shanks, J. R., Chernoff, Y. O. & Wilkinson, K. D. (2003) *J. Biol. Chem.* **278**, 52102–52115.
45. Borodovsky, A., Kessler, B. M., Casagrande, R., Overkleef, H. S., Wilkinson, K. D. & Ploegh, H. L. (2001) *EMBO J.* **20**, 5187–5196.
46. Otwinowski, Z. & Minor, W. (1997) *Methods Enzymol.* **276**, 307–326.
47. Terwilliger, T. C. & Berendzen, J. (1999) *Acta Crystallogr. D* **55**, 849–861.
48. Terwilliger, T. C. (2000) *Acta Crystallogr. D* **56**, 965–972.
49. Perrakis, A., Morris, R. M. & Lamzin, V. S. (1999) *Nat. Struct. Biol.* **6**, 458–463.
50. Jones, T. A., Zou, J. Y., Cowan, S. W. & Kjeldgaard, (1991) *Acta Crystallogr. A* **47**, 110–119.
51. Brunger, A. T., Adams, P. D., Clore, G. M., DeLano, W. L., Gros, P., Grosse-Kunstleve, R. W., Jiang, J. S., Kuszewski, J., Nilges, M., Pannu, N. S., et al. (1998) *Acta Crystallogr. D* **54**, 905–921.